AFRL-AFOSR-JP-TR-2023-0082

Advanced regional and global numerical modelling of the ionosphere to support SSA, HF radar and communication, and rocket launch monitoring

GEORGE BOWDEN
UNIVERSITY OF NEW SOUTH WALES
HIGH ST
KENSINGTON, , 2052
AUS

05/28/2023
Final Technical Report

Air Force Research Laboratory
Air Force Office of Scientific Research
Asian Office of Aerospace Research and Development
Unit 45002, APO AP 96338-5002

REPORT DOCUMENTATION PAGE

PLEASE DO NOT RETURN YOUR FORM TO THE ABOVE ORGANIZATION.

1. REPORT DATE	2. REPORT TYPE	3. DATES COVERED	
20230528	Final	START DATE 20220228	END DATE 20230227

4. TITLE AND SUBTITLE
Advanced regional and global numerical modelling of the ionosphere to support SSA, HF radar and communication, and rocket launch monitoring

5a. CONTRACT NUMBER	5b. GRANT NUMBER	5c. PROGRAM ELEMENT NUMBER
	FA2386-22-1-4003	
5d. PROJECT NUMBER	**5e. TASK NUMBER**	**5f. WORK UNIT NUMBER**

6. AUTHOR(S)
George Bowden, Melrose Brown

7. PERFORMING ORGANIZATION NAME(S) AND ADDRESS(ES)
UNIVERSITY OF NEW SOUTH WALES
HIGH ST
KENSINGTON 2052
AUS

8. PERFORMING ORGANIZATION REPORT NUMBER

9. SPONSORING/MONITORING AGENCY NAME(S) AND ADDRESS(ES)	10. SPONSOR/MONITOR'S ACRONYM(S)	11. SPONSOR/MONITOR'S REPORT NUMBER(S)
AOARD UNIT 45002 APO AP 96338-5002	AFRL/AFOSR IOA	AFRL-AFOSR-JP-TR-2023-0082

12. DISTRIBUTION/AVAILABILITY STATEMENT
A Distribution Unlimited: PB Public Release

13. SUPPLEMENTARY NOTES

14. ABSTRACT
Chemical output from rocket launches produce measurable disturbances in the ionosphere. This was project aimed at improving models for accurately estimating global ionosphere states and their regional perturbations due to rocket launches. The models are multi-faceted including subroutines for regional general circulation model (GCM), a Stochastic Parallel Rarefied-gas Time-accurate Analyzer (SPARTA) and Global Ionosphere Thermosphere Model (GITM). By combining these tools a total electron count could be predicted to be compared with experimental data. The models show good agreement to show that this is a viable approach. We are now looking at transitioning this research to AFRL/RV to see if they can find a way to exploit the models in future operational systems.

15. SUBJECT TERMS

16. SECURITY CLASSIFICATION OF:			17. LIMITATION OF ABSTRACT	18. NUMBER OF PAGES
a. REPORT U	b. ABSTRACT U	c. THIS PAGE U	SAR	30

19a. NAME OF RESPONSIBLE PERSON	19b. PHONE NUMBER *(Include area code)*
GEOFFREY ANDERSEN	

Standard Form 298 (Rev.5/2020)
Prescribed by ANSI Std. Z39.18

Report for AOARD Grant FA2386-22-1-4003

"Advanced regional and global numerical modelling of the ionosphere to support SSA, HF radar and communication, and rocket launch monitoring"

May 28, 2023

Name of Principal Investigators (PI and Co-PIs):

- E-mail address: g.bowden@adfa.edu.au
- Institution: University of New South Wales, Canberra
- Mailing Address: School of Engineering and Information Technology, The University of New South Wales, Canberra, 2612, ACT, Australia
- Phone: +61 2 5114 5285

- E-mail address: melrose.brown@adfa.edu.au
- Institution: University of New South Wales, Canberra
- Mailing Address: School of Engineering and Information Technology, The University of New South Wales, Canberra, 2612, ACT, Australia
- Phone: +61 2 5114 5129

Period of Performance: 02/28/2023 – 02/27/2023

Abstract:
Rockets cause ionospheric disturbances as they pass through the upper atmosphere. Better understanding these disturbances offers potential for new methods for launch detection and characterization and insight into ionospheric and thermospheric physics. A grant was provided to develop numerical models to accurately estimate the effect of rocket launches on the ionosphere. This project included use of data assimilation for the global state of the ionosphere-thermosphere system, direct simulation Monte Carlo (DSMC) modelling the rocket exhaust plume, and general circulation model (GCM) modelling for regional ionosphere-thermosphere impacts of the plume. Data assimilation of space weather index biases based on time weighted accumulations was assessed. Ionospheric depletions associated with a small-lift launch vehicle (a Rocket Lab Electron) were modelled using a GCM and compared with observations, which produced similar results for total electron count changes. Ionospheric waves were modelled by perturbing GCM boundary conditions, producing ionospheric waves with similar spatial profiles.

Report:

Introduction

Space launches generate observable perturbations to the ionosphere through several mechanisms (Mendillo, 1981). Due to the rarified upper atmosphere, these effects can manifest over many hundreds of kilometers. Chemicals present in rocket exhaust, such as water vapor, provide a more rapid pathway for ionospheric recombination reducing electron densities. Interaction of the rocket plume with the thermosphere also produces acoustic and gravity waves which perturb the ionosphere. These phenomena can provide a novel test of numerical models of the upper atmosphere. Moreover, they may potentially serve as a means of detecting and characterizing rocket launches.

Prior to the work described here, the investigators explored the use of regional general circulation model (GCM) simulations to model ionospheric depletions due to rocket launches (Bowden, Lorrain, & Brown, 2020). This work employed the Global Ionosphere Thermosphere Model (GITM) (Ridley, Deng, & Toth, 2006). The chemical model in the

GCM was extended to include the effects of charge exchange and recombination reactions between chemical species present in rocket exhaust and the ionosphere. Source terms were added to simulations along the rocket trajectories, based on analytic models for initial plume diffusion. This approach reproduced the observed diameter and movement of the depletion well for the cases examined but overestimated the observed reduction in ionospheric densities. It was determined that more accurate specification of the background ionosphere and rocket exhaust plume were required to better predict the ionospheric perturbation.

Following this initial work, a grant was provided for the development of numerical methods to accurately determine ionospheric perturbations due to rocket launches. Different aspects of the work were intended to focus on estimating the global ionosphere state, modelling the rocket plume interaction with the thermosphere, and modelling the regional ionospheric response to perturbations. Comparison between modelling and simulation was also performed over the course of the project. Progress in each of these areas is reported here.

Ionosphere State Estimation

Part of this work was aimed at improving estimates of background ionospheric conditions. This study used an ensemble Kalman filtering (EnKF) approach with the TIE-GCM model of the ionosphere-thermosphere system (Richmond, Ridley, & Roble, 1992). In the EnKF algorithm, an ensemble of model states represents the estimated state of a physical system (as the ensemble mean) and its uncertainty (as the ensemble variance). These states are alternately advanced forward in time using the model and then updated based on observations. The latter step adjusts the posterior ensemble mean and variance to match a Bayesian estimate considering the prior ensemble mean and variance and the observation values and uncertainties.

The Data Assimilation Research Testbed (DART) was used to implement the EnKF algorithm (Anderson, et al., 2009). The EnKF has previously been implemented for TIEGCM using DART, for example by Matsuo (2014). Programs which interface with TIE-GCM are included in the DART distribution. Prior to the current work, the investigators had implemented scripts to set up and run EnKF data assimilation experiments on the National Computational Infrastructure (NCI) computing clusters.

A novel data assimilation approach was investigated in which appropriate biases for space weaher indices were estimated as part of the state. In addition to data for variables such as temperature, the state included a bias for the solar flux $F_{10.7}$ and geomagnetic a_p indices. It was hoped that estimating and applying these biases would allow the ensemble to retain information from observations and enable accurate prediction over longer timescales. The investigators had previously observed that in the absence of new observations EnKF TIE-GCM state estimates would quickly revert to those without filtering (over timescales of several hours).

It was discovered that the EnKF algorithm overestimated the required changes in biases. If an adjustment was made to these indices, the full effect of the change was not represented at the next timestep when the algorithm evaluated the further changes required. This overestimate resulted in stability issues. To counter the problem, time weighted accumulations were used to represent the bias in the ensemble states, similar to the indices described by Wrenn (1987). The a_p bias accumulation, $\delta\tilde{a}_p$, was defined such that:

$$\delta\tilde{a}_p(t_i) = \left(1 - \exp\left(-\frac{\delta t}{\tau}\right)\right)\delta\tilde{a}_p(t_{i-1}) + \exp\left(-\frac{\delta t}{\tau}\right)\delta a_p(t_{i-1}),$$

where δt is the timestep of the algorithm and τ is a time constant indicating how long the accumulation is affected by a particular bias value. Here $\delta a_p(t_{i-1})$ represents the posterior

value for δa_p calculated for time step $i-1$ and applied by the model over that time step. A similar definition applied for the $F_{10.7}$ bias accumulation.

Test cases were examined assimilating density data from the CHAMP and GRACE accelerometers (Mehta, Walker, Sutton, & Godinez, 2017). Data assimilation experiments were performed using a 90 member ensemble with an inflation factor of 2.0. Results of experiments examining the period from 0:00 UTC September 12 2003, to 0:00 UTC September 22 2003 are shown in Figure 1. This period included a geomagnetic storm which peaked on September 17. Unfortunately, the data assimilation method did not show a clear advantage over using TIE-GCM without filtering. It was noted that use of a longer time constant reduced accuracy prior to the storm and a shorter time constant reduced accuracy following the storm. It appears that the biases do not represent persistent differences between TIE-GCM and the observed thermosphere as initially hypothesized. Rather, they are associated with reduced fidelity when solar and geomagnetic conditions change.

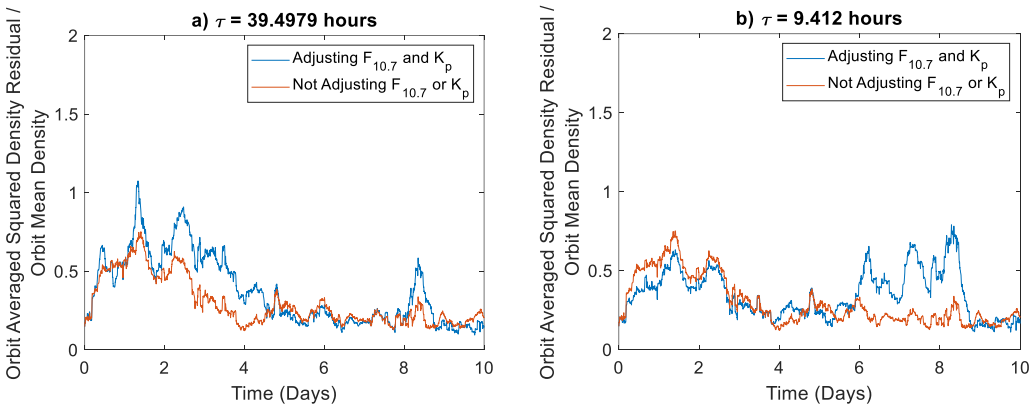

Figure 1 Ratio of orbit averaged density residual to orbit averaged density for TIE-GCM estimates of CHAMP accelerometer density measurements. The blue lines apply biases to space weather indices estimated using the EnKF algorithm the orange lines use the indices without adjustments. Figure a) and b) show results for different time constants.

Rocket Plume Expansion

The Stochastic Parallel Rarefied-gas Time-accurate Analyzer (SPARTA) code was applied to analyze initial expansion of the rocket exhaust plume (Gallis, Torczynski, Plimpton, Rader, & Koehler, 2014). This code applies the DSMC technique to analyze rarefied gas flows in either two- or three-dimensions. In SPARTA simulations, a stochastically generated set of particles are moved through a hierarchical cartesian grid which is used to determine the effect of collisions and reaction rates.

Two-dimensional SPARTA simulations of rocket plumes in the thermosphere have been performed for both uniform and stratified thermospheres. In each case, the simulation covered a 200 km × 400 km domain in the vertical and horizontal directions respectively. The thermosphere consisted of a mixture of 0.036% O_2, 18.12% N_2, and 81.52% O, while the rocket exhaust consisted of 32% N2, 28% H_2O, 25% H_2, and 15% CO_2. This was similar to the case studied by Kaplan & Bernhardt (2010).

The location of the rocket was fixed at the midpoint of the left boundary. Horizontal travel with fixed speed was represented by specifying initial velocities for particles entering the simulation domain from this boundary with a specified velocity to the right. Density and temperature for the incoming thermosphere particles in the uniform simulation are listed in Table 1. In the stratified simulation the thermosphere densities were adjusted to give a scale

height of 60 km while maintaining the same density at the scale height.

	Velocity ($m.s^{-1}$)	**Density ($kg.m^{-3}$)**	**Temperature (K)**
Thermosphere	7720.0000	2.360E+20	809.0000
Exhaust	10790.0000	1.104E+15	120.0000

Table 1 SPARTA simulation parameters for the uniform thermosphere case.

A snapshot from the stratified thermosphere simulation is shown in Figure 2. The simulation involved a total of 285 million particles and used 243 CPU hours on the NCI Gadi cluster. Future development will include implementation of:

- boundary conditions from realistic thermosphere models,
- collisions,
- gravitational and non-inertial forces, and
- varying rocket altitude and velocity.

Postprocessing will be developed to determine the density, composition, and velocity of the rocket exhaust exiting the simulation domain. These will be used as inputs for the GCM simulation of the thermosphere.

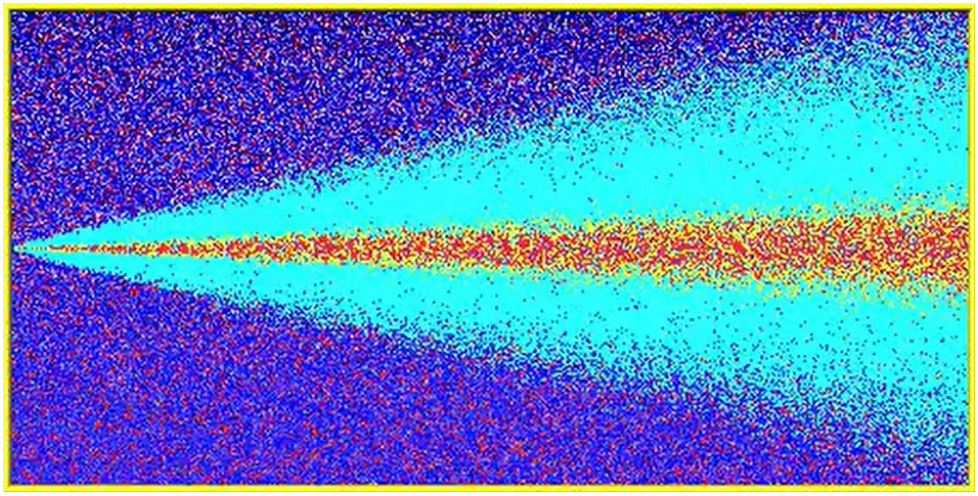

Figure 2 Particles in the SPARTA simulation of a rocket exhaust plume with a stratified thermosphere.

Regional Ionospheric Depletion Modelling

This numerical modelling method previously developed by Bowden, Lorrain, & Brown (2020) was employed to study the ionospheric perturbation caused by the launch of a Rocket Lab Electron launch vehicle on March 22, 2021. The manuscript describing this work is attached. The new capability which was developed in this case was the calculation of slant total electron content (TEC). This enabled direct comparison with ionospheric delay measurements for individual satellites. Doing so allowed finer scale comparison between modelling and observation than was previously achieved using vertical TEC maps, which obscure details due to binning and approximation of the ionosphere as a shell at fixed height (Rideout & Coster, 2006).

The Electron launch helped to better understand the capabilities and limitations of the GCM approach to ionospheric depletion modelling. In this case, unlike the one examined previously, the maximum decreases in TEC were similar in both observation and modelling. However, observations indicated that advection was not modelled correctly, leading to an inaccurate estimation of the unperturbed ionospheric density and movement of the depletion

over time. A method of better modelling thermospheric and ionospheric advection in future may be to employ a version of GITM with regional grid refinement (Deng, et al., 2021).

Regional Ionospheric Wave Modelling
GCM modelling was also used to examine ionospheric perturbations due to acoustic waves, following on from prior work (Bowden & Brown, 2019; Bowden & Brown, 2021). In the current work, perturbed boundary conditions were implemented in GITM to represent these waves. Separate simulations were done for waves propagating into the upper and lower thermosphere. Perturbations to the boundary conditions in each case were determined by propagating acoustic rays from the rocket to those surfaces. A conference paper describing this work is attached.

The GCM produced a similar V-shaped ionospheric perturbation to ray tracing simulations and TEC observations reported by Lin, et al. (2017). The speed of propagation for the disturbances was comparable with observation. However, the magnitudes of TEC perturbations were substantially smaller than those observed. Issues identified included the gap in altitudes between the upper and lower thermosphere simulations and numerical diffusion from GITM's advection scheme. In future, GCM modelling of ionospheric waves could be improved by fully specifying the thermosphere state based on ray-tracing derived perturbations to an empirical model.

List of Publications and any Significant Collaborations that resulted from your AOARD-supported project <u>for this year of the project</u>:
The following paper was accepted for publication in peer-reviewed conference proceedings:

- Bowden, G. W., Numerical Simulation of Rocket Generated Travelling Ionospheric Disturbances Using a General Circulation Model, *Proceedings of the 20th Australian Space Research Conference*, September 26 – September 28, 2022

The following manuscript is currently under review:

- Bowden, G. W., & Brown, M., Numerical Modelling and GNSS Observations of Ionospheric Depletions due to a Small-Lift Launch Vehicle, submitted to *Space Weather*, 2023

Attachments: The above publication and pre-print are attached.

Bibliography

Anderson, J. A., Hoar, T., Raeder, K., Liu, H., Collins, N., Torn, R., & Avellano, A. (2009). The data assimilation research testbed: A community facility. *Bulletin of the American Meteorological Society*, 1283-1296.

Bowden, G. W., & Brown, M. (2019, December). Numerical Simulation of the Ionospheric Response to Acoustic Waves Generated by Spacecraft Launches. *American Geophysical Union, Fall Meeting 2019.* San Francisco.

Bowden, G. W., Lorrain, P., & Brown, M. (2020). Numerical Simulation of Ionospheric Depletions Resulting From Rocket Launches Using a General Circulation Model. *Journal of Geophysical Research: Space Physics*, e2020JA027836.

Bowden, G., & Brown, M. (2021). Numerical simulations of the ionospheric response to atmospheric waves generated by the launch of rockets. *43rd COSPAR Scientific Assembly.* Sydney.

Deng, Y., Zhu, Q., Lin, C., Jin, M., Liu, C., & Sheng, C. (2021). Electric field variability and impact on the ionosphere-thermosphere. In Y. Nishimura, O. Verkhoglyadova, Y. Deng, & S. Zhang, *Cross-Scale Coupling and Energy Transfer in the Magnetosphere–Ionosphere–Thermosphere System.*

Gallis, M. A., Torczynski, J. R., Plimpton, S. J., Rader, D. J., & Koehler, T. (2014). Direct

Simulation Monte Carlo: The Quest for Speed. *Proceedings of the 29th International Symposium on Rarefied Gas Dynamics*, (pp. 27-36).

Kaplan, C. R., & Bernhardt, P. A. (2010). Effect of an Altitude-Dependent Background Atmosphere on Shuttle Plumes. *Journal of Spacecraft and Rockets*, 700-703.

Lin, C. C., Shen, M. H., Chou, M. Y., Chen, C. H., Yue, J., Chen, P. C., & Matsumura, M. (2017). Concentric traveling ionospheric disturbances triggered by the launch of a SpaceX Falcon 9 rocket. *Geophysical Research Letters*, 7578-7586.

Matsuo, T. (2014). Upper atmosphere data assimilation with an ensemble Kalman filter. *Modeling the Ionosphere–Thermosphere System*, 273-282.

Mehta, P. M., Walker, A. C., Sutton, E. K., & Godinez, H. C. (2017). New density estimates derived using accelerometers on board the CHAMP and GRACE satellites. *Space Weather*, 558-576.

Mendillo, M. (1981). The Effect of Rocket Launches on the Ionosphere. *Advances in Space Research*, 275-290.

Richmond, A. D., Ridley, E. C., & Roble, R. G. (1992). A thermosphere/ionosphere general circulation model with coupled electrodynamics. *Geophysical Research Letters*, 601-604.

Rideout, W., & Coster, A. (2006). Automated GPS processing for global total electron content data. *GPS solutions*, 219-228.

Ridley, A. J., Deng, Y., & Toth, G. (2006). The global ionosphere–thermosphere model. *Journal of Atmospheric and Solar-Terrestrial Physics*, 839-864.

Wrenn, G. L. (1987). Time-Weighted Accumulations ap(τ) and Kp(τ). *Journal of Geophysical Research*, 10125-10129.

Numerical Modelling and GNSS Observations of Ionospheric Depletions due to a Small-Lift Launch Vehicle

G. W. Bowden [1], **M. Brown** [1]

[1]School of Engineering and Information Technology, University of New South Wales Canberra, Campbell, ACT, Australia

Key Points:

- Ionospheric effects of the Rocket Lab Electron launch of 22 March, 2021 were investigated
- Numerical modelling using GITM and navigation satellite signal observations showed comparable ionospheric depletions

Corresponding author: George Bowden, g.bowden@adfa.edu.au

Abstract

Space launches produce ionospheric disturbances which can be observed through measurements such as Global Navigation Satellite System signal delays. Here we report observations and numerical simulations of the ionospheric depletion due to a Small-Lift Launch Vehicle. The case examined was the launch of a Rocket Lab Electron at 22:30 UTC on March 22, 2021. Despite the very small launch vehicle, ground stations in the Chatham Islands measured decreases in line-of-sight total electron content for navigation satellite signals following the launch. General Circulation Model results indicated ionospheric depletions which were comparable with these measurements. Line-of-sight measurements showed a maximum decrease of 2.7 TECU in vertical total electron content, compared with a simulated decrease of 2.6 TECU. Advection of the exhaust plume due to its initial velocity and subsequent effects of neutral winds are identified as some remaining challenges for this form of modelling.

Plain Language Summary

The ionosphere is a region of the upper atmosphere containing a mixture of ions and electrons. Chemicals released when rockets pass through this region allow ions and electrons to recombine, reducing their concentrations. These reductions were measured for the launch of a Rocket Lab Electron rocket. The measurements were made based on the difference in time signals at different frequencies took to pass through the ionosphere, which indicated its concentration. Computer simulations were carried out for this case, which showed a similar decrease in the concentration of the ionosphere following launch to the the measurements. Some potential improvements to the models are suggested based on this work.

1 Introduction

During space launch, rockets release exhaust gasses which modify the ionosphere. The exhaust includes heteronuclear molecules such as CO_2 and H_2O, which undergo rapid charge exchange reactions with O^+ in the F_2-region to form molecular ions (Mendillo, 1981). These ions readily undergo neutralisation reactions, reducing ionospheric electron densities. Ionospheric depletions following rocket launches have been observed using a variety of methods, including ionosonde soundings (Booker, 1961), Faraday rotation of satellite signals (Mendillo et al., 1975), air glow images (Mendillo & Baumgardner, 1982), incoherent scatter radar measurements (Wand & Mendillo, 1984), Global Navigation Satellite System (GNSS) signal delays (Furuya & Heki, 2008), and satellite Langmuir probe measurements (Park et al., 2016). These depletions can provide a means of investigating ionospheric physics or detecting and characterising launches.

In this study, we investigate ionospheric depletions due to the launch of an Rocket Lab Electron launch vehicle. This three-stage partially recoverable Small-Lift Launch Vehicle (SLLV) has a wet mass of $13,000$ kg and carries payloads of up to 300 kg to low-Earth orbit (LEO) (Rocket Lab, 2022). Both stages use an RP-1/LOX propellant mixture. Observations of ionospheric depletions were first made for the launch of the Vanguard SLV-4 rocket, a comparably sized SLLV (Booker, 1961). However, ionospheric effects of such small launch vehicles have not previously been simulated numerically or observed in GNSS data.

The launch (mission name "They Go Up So Fast") occurred at 22:30 UTC on March 22, 2021, corresponding to 11:15 Chatham Standard Time (CHAST). Rocket Lab Launch Complex 1 was the launch site, located at 39.262°S, 177.865°E (on the Māhia Peninsula, New Zealand). The launch vehicle carried 7 small satellites to target altitudes between 450 km-550 km and 45.0° inclination. Section 2 and 3 respectively outline the numerical ionosphere-thermosphere system modelling and GNSS observation methods applied

to the "They Go Up So Fast" launch case. Results of these investigations are detailed in Section 4 and further discussed in Section 5.

2 Numerical Modelling

A numerical simulation of the ionospheric depletion due to the rocket launch was performed using the Global Ionosphere Thermosphere Model (GITM) (Ridley et al., 2006) adopting the methods outlined by Bowden et al. (2020). This simulation covered an 8-hour period from 22:30 UTC on March 22 to 06:30 UTC on March 23. The chosen domain spanned 50°S to 30°S in latitude, 170°E to 155°W in longitude, and 100 km to 536.67 km in altitude. This domain was covered by a regular 108×144 grid horizontally and 50 grid points vertically. These altitudes corresponded to the thermosphere (in the neutral atmosphere) and E- and F-regions (in the ionosphere). The simulation was run both with and without rocket exhaust gasses being added. The electon density integrated along the line-of-sight, or Slant Total Electron Count (STEC), was computed for GNSS satellites based on azimuth and elevation data from the source described in Section 3. Output was taken at 300 s intervals.

The rocket trajectory was estimated based on the target orbit, altitude, and speed data. Rocket Lab provide speed and altitude data in their launch video (Rocket Lab, 2021). These data indicated that passage through the simulation domain coincided with the second stage firing. The total mass flow rate during the second stage firing was estimated based on a nominal thrust of $T = 25.8$ kN and specific impulse of $I_{sp} = 343$ s using $\dot{m} = T/\left(I_{sp} g_0\right)$ (Rocket Lab, 2022). This was divided between H_2O and CO_2 assuming complete combustion. The rocket chemical source was added at points along the trajectory for 520 s following launch (approximately corresponding to second stage cut-off at approximately 320 km altitude). These were added following 300 s delay during which diffusion was modelled analytically, avoiding excessive concentration gradients which cause problems for the GITM numerical solver (Bowden et al., 2020).

3 GNSS Observations

Changes in Total Electron Content (TEC) following the launch were measured from the Chatham Islands reference station (CHTI), located at 43.735°S, 176.617°E, 75.764 m altitude. Slant TEC (STEC) data for the CHTI station were obtained from the Madrigal CEDAR database. These were available for both GPS (here numbered 1 to 31) and GLONASS (numbered 32 to 55) satellites. Data also included estimated pierce point locations, which are plotted in Figure 1, and azimuth and elevation data. To approximate Vertical TEC (VTEC), STEC data were multiplied by $\sin(\alpha)$, where α was the elevation angle of the satellite measured at the ground station. This quantity will be referred to here as Pseudo-VTEC (PVTEC). Data were recorded at 30 s intervals, though the time series was interspersed with brief gaps in availability.

The trajectory of the rocket passed to the north of the islands and is shown in Figure 1. In the 90 minutes following launch, satellite 15, satellite 29, and satellite 55 pierce points were identified as crossing the rocket ground track and selected for further study. As shown in Figure 2, the crossing occurred earliest for satellite 15, followed by satellite 55, and then satellite 29.

To provide comparison with an undisturbed ionosphere, data at a time offset of 1 day (i.e. at the same time of day for March 23) were also considered. Levels of solar activity were similarly low for both days, with observed Penticton $F_{10.7}$ solar flux index of 80 SFU and 79 SFU on the launch and following day respectively (Tapping, 2013). There were no flares of Class C or greater on either day. Geomagnetic activity was also low on both days, with the Potsdam K_p index not exceeding 3+ on either day (Matzka et al., 2021). As the orbital period of GNSS satellites is half a sidereal day, the ground track

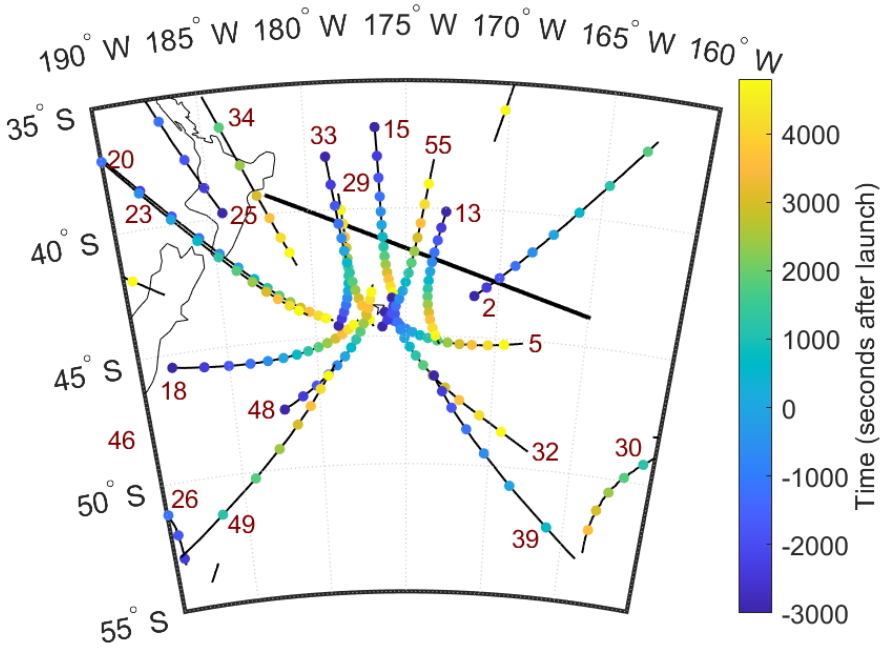

Figure 1: Pierce points for TEC measurements from the Chatham Islands GNSS ground station (CHTI) between 21:40 and 24:00 UTC. Markers are plotted at 10 minute intervals The estimated rocket ground track while the first and second stages were firing is indicated by the thick black line.

of each GPS satellite approximately repeats from one day to the next. By contrast, the ratio of the orbital period of GLONASS satellites to a sidereal day is approximately 8/17. Because 8 GLONASS satellites orbit in each plane, a satellite will approximately repeat the ground track traced by the preceding satellite the previous day. Thus, data for satellite 55 on the launch day could be compared with those for satellite 48 the following day.

TEC data from the OWMG reference station, located at 44.024°S, 176.369°E, 21.620 m altitude, were also analysed. The features of these data were very similar to those of the nearby CHTI station, supporting the same conclusions but not providing additional information. Therefore, OWMG station data are not presented here.

4 Results

The initial expansion and subsequent decay of the simulated ionospheric depletion is shown in Figure 3. Shortly after launch, the VTEC depletion was highly elongated and was aligned with the rocket ground track. At later times the depletion expanded perpendicular to the ground track while the magnitude at its centre decreased. Comparing simulations with and without rocket exhaust, the largest VTEC depletion was 3.46 TECU, occurring at 23:30. The background VTEC in the simulation increases and becomes more spatially uniform as local time progresses from late morning to mid afternoon (11:15 to 14:45 CHAST).

Figures 4, 5, and 6 compare the GITM output with GNSS measurements taken at the CHTI ground station. In each case, GITM output is shown with and without rocket exhaust gasses while GITM observations are shown on the day of launch and following day. Evidence of a depletion in STEC$\times\sin(\alpha)$ was found for GNSS data following the

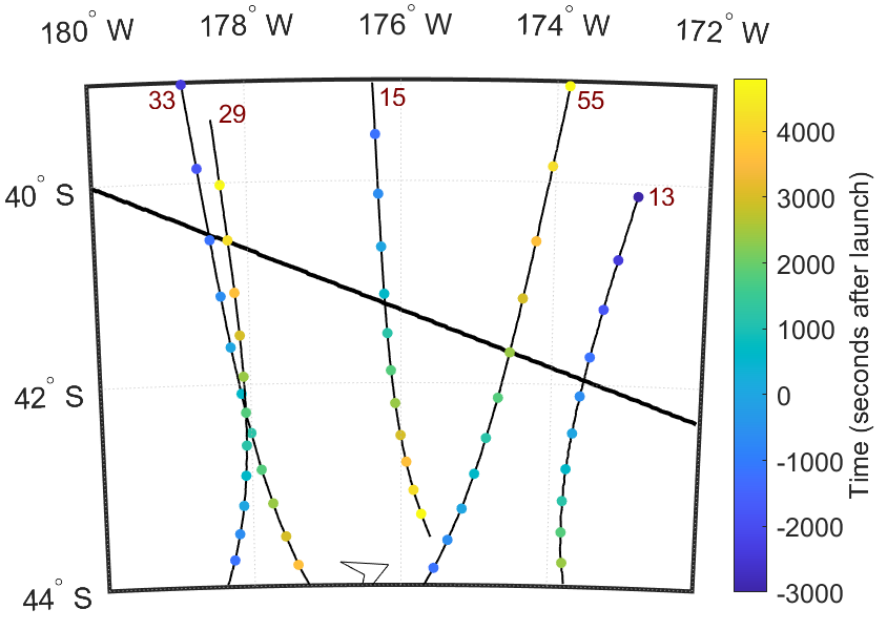

Figure 2: Similar to Figure 1, zoomed in around pierce point crossings of the ground track.

launch in each case. The depletion appears earliest for satellite 15, followed by satellite 55, and then satellite 29.

The estimated pierce point for satellite 15 observations crossed the ground track at approximately 22:40 UTC, heading southward. Therefore, STEC measurements around this time reflected ionosphere changes near the centre of the exhaust plume shortly after passage of the rocket. Figure 4 shows that a sudden variation in the rate of change in PVTEC occurred around 22:40 UTC for both simulated GITM and real GNSS observations. Between 22:40 and 22:50 UTC, the observed quantity changes at approximately -0.1 TECU.min^{-1}. During the same period, the difference between the simulated quantity with and without exhaust changed at approximately -0.05 TECU.min^{-1}. The background value of PVTEC steadily increased in the simulation without exhaust, but declined slightly in the real data offset by 1 day.

For satellite 55 observations, the pierce point crossed the ground track at approximately 23:10 UTC. Figure 5 shows that this crossing approximately coincided with a minimum in PVTEC for the GITM simulation. However, the real GNSS observations indicate that the minimum occurred earlier, at 23:02 UTC. The simulated maximum depletion was 2.6 TECU while the observed maximum (based on the difference between the 1 day offset and post-launch data) was 2.7 TECU. The depletion in the simulated quantity was apparent ($> 1\%$ of maximum value) in the GITM simulations between 22:45 and 23:45 UTC. Significant differences between the real GNSS data and those offset by 1 day were observed for approximately the same time period.

In the case of satellite 29, the ground track crossing occurred at approximately 23:40 UTC. However, the minimum in PVTEC for the GITM simulation occurred earlier at 23:20 UTC. Observed values of this quantity had a minimum at 23:14 UTC. The maximum depletion based on the simulations was 0.9 TECU, while the maximum depletion based on observations (determined as above) was 2.6 TECU. The depletion appeared in simulated

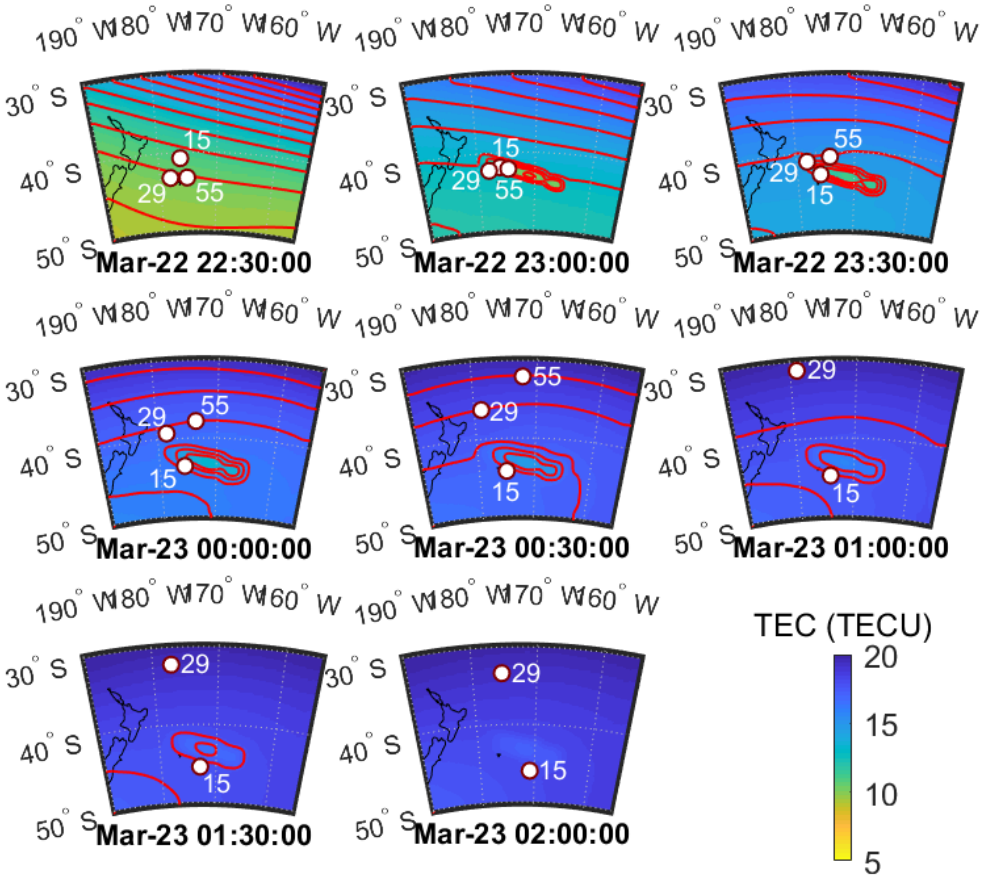

Figure 3: VTEC maps from the GITM simulation of the Electron launch at 22:30 UTC on March 22, 2021. Red contour lines occur at intervals of 1 TECU $\equiv$ 10^{16}electrons.m^{-2}. Estimated ionospheric pierce points for satellites 15, 55, and 29 are overlayed.

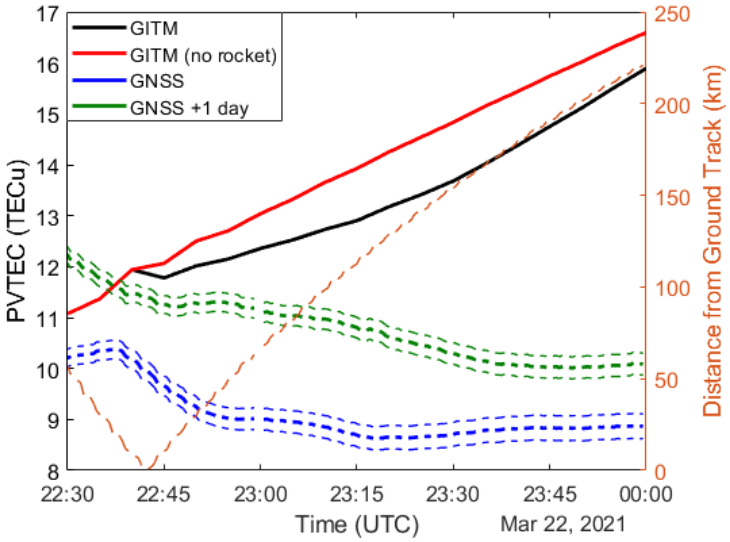

Figure 4: PVTEC measured at the CHTI ground station for GNSS satellite 15. Simulated results from GITM with (black line) and without (red line) the addition of rocket exhaust are shown for a 90-minute period following the launch. GNSS measurements from the satellite (blue lines) and comparable measurements from the next day (green lines) are also provided. Mean value (thick line) and upper and lower bounds (thin lines) are plotted for the GNSS measurements. Estimated distance from the pierce point to the ground track is also indicated (thin orange line, right axis)

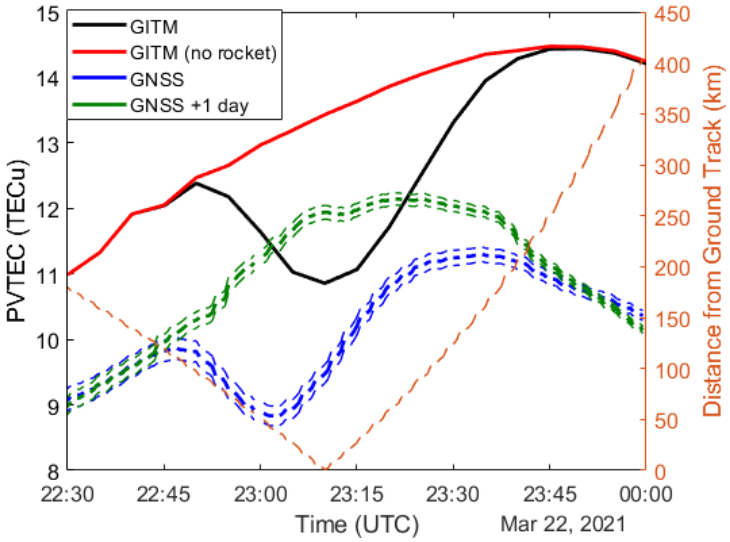

Figure 5: Similar to Figure 4 for GNSS satellite 55 (black, red, and blue lines) and satellite 48 (green lines).

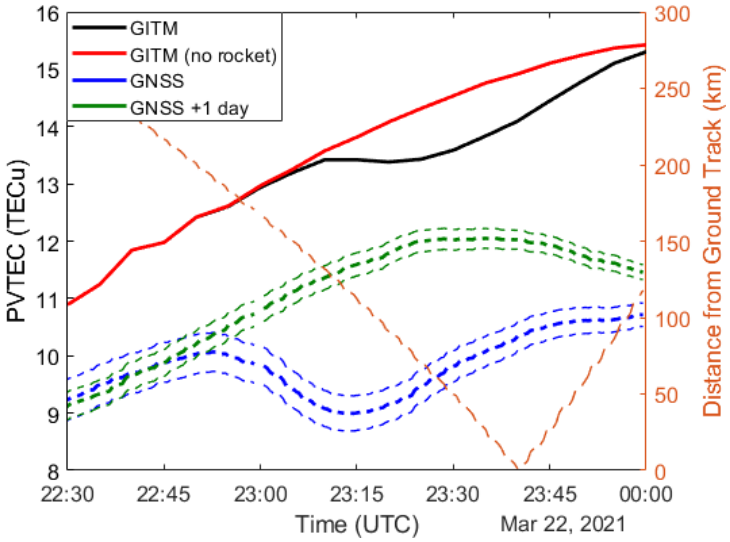

Figure 6: Similar to Figure 4 for GNSS satellite 29.

data from 23:00 UTC onwards (at $> 1\%$ of maximum value) and significant differences between real GNSS data and those offset by 1 day appeared at approximately this time.

Global evolution of the depletion is illustrated by plotting changes in the total numbers of exhaust molecules and electrons in Figure 7. We define $-\Delta N_e$, ΔN_{CO_2}, and ΔN_{H_2O} as the respective differences in the number of electrons, CO_2 molecules, and H_2O molecules due to the addition of rocket exhaust. Only electrons and molecules above 200 km are considered, as significant ionospheric depletions are limited to this region and GITM introduces unrealistic changes in concentrations near the lower boundary at 100 km (Bowden et al., 2020). ΔN_{CO_2}, and ΔN_{H_2O} both decreased rapidly from their initial value after deposition by the rocket. This resulted in a maximum in ΔN_e of approximately 8.2×10^{27} at 00:05 UTC on March 23. Subsequently, ΔN_e decayed with a characteristic time of $\tau \approx 2$ to 3 hours ($\frac{1}{\tau} = \frac{1}{\delta n}\frac{d\Delta n}{\delta t}$).

Simulated changes in the number of exhaust molecules and electrons across different altitudes resulting from addition of rocket exhaust are shown in Figure 8. We define $-\lambda_e$, λ_{CO_2}, and λ_{H_2O} as the respective differences in the number of electrons, CO_2 molecules, and H_2O molecules per unit altitude due to the addition of rocket exhaust. Both CO_2 and H_2O concentration increases were initially peaked around 270 km altitude before falling to lower altitudes. Electron concentration decreases were initially concentrated around similar altitudes, before they diffused to higher altitudes over subsequent hours. These decreases tended to persist for longer times at higher altitudes.

5 Discussion

The observations and simulations presented in Section 4 showed that ionospheric effects of even comparatively small launch vehicles such as the Electron are detectable through GNSS observations. Both real and simulated measurements evidinced ionospheric depletions larger than the uncertainty for these measurements. These results suggest that observations from GNSS ground stations are sufficiently sensitive to detect most space launch vehicles as they pass through F-region altitudes. Numerical simulations could be

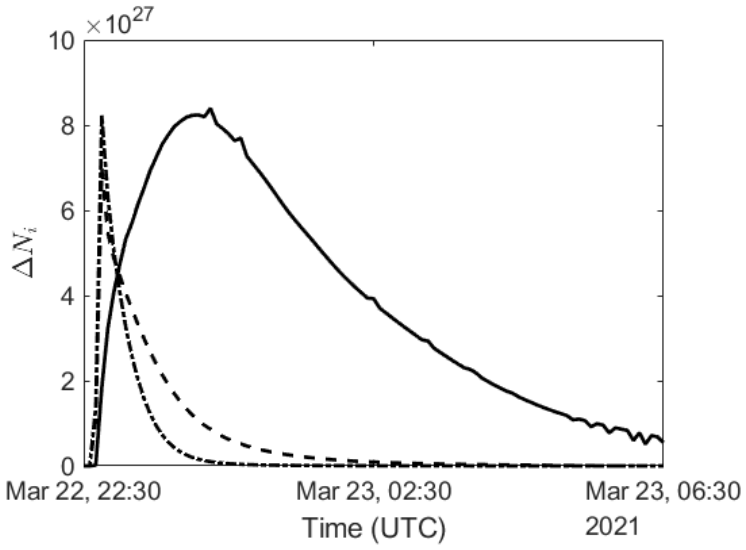

Figure 7: Changes in the total number of electrons and exhaust molecules above 200 km altitude in the GITM simulation due to the rocket. ΔN_e (solid line), ΔN_{CO_2} (dashed line), and $\Delta N_{\mathrm{H}_2\mathrm{O}}$ (dash-dotted line) are shown.

used in future to provide data for a classification scheme to determine when launches occur using GNSS observations.

Our method provides better agreement with observations of the magnitude of TEC depletion in the current case than it did for the Falcon 9 launch of FORMOSAT-5 which was investigated previously (Bowden et al., 2020). This can be attributed to the shallower angle of ascent for the case presented in this paper. Consequently, the vertical component of initial plume velocity was lower in the Electron case and therefore ignoring the consequent vertical advection of CO_2 and H_2O molecules in the simulations is more realistic. Lower altitudes corresponded to decreased thermosphere residence times for the molecules. Moreover, ionosphere production rates increase with decreasing altitude in the F-region. Together these effects result in a shorter-lived ionospheric depletion (comparing Figure 7 with Figure 10(b) in Bowden et al. (2020)). In future, satellite-based GNSS radio occultation may provide opportunities to study the evolution in the depletion at higher altitudes more directly.

Advection of rocket exhaust due to its initial velocity in the horizontal direction may have been important in the Electron case. This may help explain why the depletion appeared to have been underestimated by GITM for the satellite 29 observations but not those for satellite 55. Figure 1 shows that the pierce point for the former satellite passed closer to the launch site. The Electron I_{sp} value corresponded to an exhaust velocity of $v_e = 3360$ m.s^{-1}. The launch vehicle was estimated to reach this speed approximately 297 s after launch when located at 40.88°S, 177.31°W. Prior to this time, exhaust would have had an initial velocity opposite that of the launch vehicle (in an Earth Centred Earth-fixed reference frame).

The launch of an Electron SLLV better approximates our model of initial plume expansion as a series of point releases than those of larger launch vehicles. Plume dimensions are reduced for smaller launch vehicles, with an approximate analytical treatment indicating length and maximum radius are each proportional to $\sqrt{T}$ where T is thrust (Jarvinen et al., 1966). Moreover, forces exerted by smaller launch vehicles on the back-

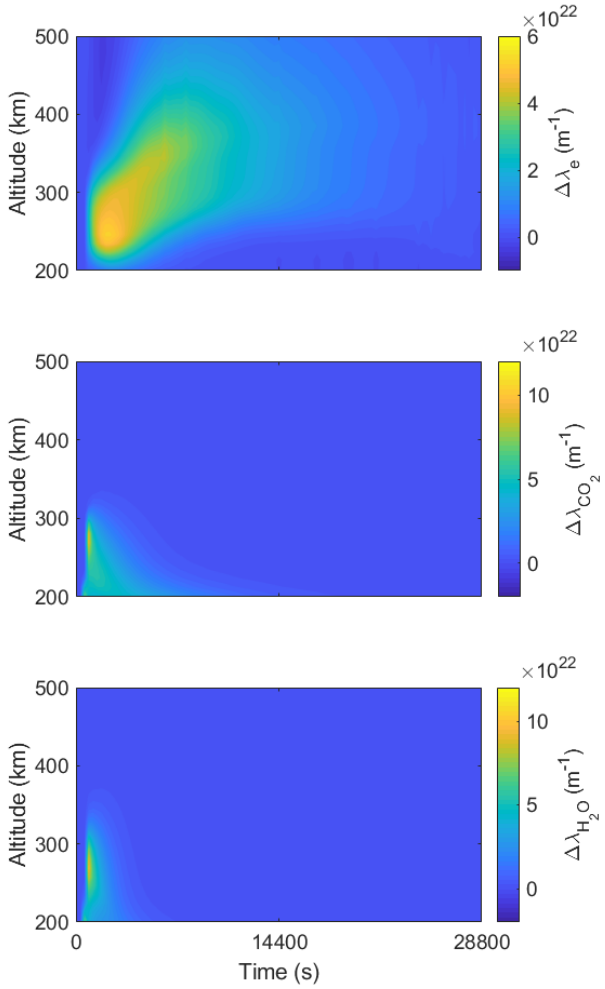

Figure 8: Altitude distribution of changes in the number of (a) electrons, (b) CO_2 molecules, and (c) H_2O molecules over time.

ground ionosphere and thermosphere are expected to affect the background state less. Resulting disturbances such as the "snow-plow effect", wherein the plume directly displaces the ionosphere, are thus minimised.

For smaller launch vehicles initial high concentrations of exhaust gasses are less likely to saturate the ionosphere, reducing electron and ion concentrations to very low levels thereby inhibiting these gasses further contribution to the depletion. Therefore, in such cases, numerical models will be less sensitive to the treatment of the early expansion of the plume. It will also limit the opportunity exhaust gasses have to diffuse to higher altitudes where they can give rise to long-lived ionospheric depletions. Figure 7 shows that time that exhaust gasses spent within the thermosphere in the simulation was short compared with that for which the depletion existed (ΔN_{CO_2} and ΔN_{H_2O} declined below 10% of peak levels 95 min and 65 min after launch respectively) for the Electron launch. The exhaust gasses declined more rapidly in simulations for this case than for either Falcon 9 launch examined by Bowden et al. (2020) (see Figure 10 in the reference).

The minima in PVTEC observations of satellites 55 and 29 occurred earlier than their pierce points crossed the satellite track. Therefore, the depletion appears to have been pushed southwards towards the CHTI ground station due to advection of rocket exhaust gasses by thermospheric winds. GITM estimated that minima occurred later, suggesting the model underestimated the southward component of these winds.

The regional GITM simulations in this study did not include global-scale convection, which affects neutral wind and ion drift velocities. Open boundary conditions at the upper and lower bounds for latitude and longitude were applied in these simulations, which produces unrealistic results for longer simulations. Figure 3 shows that latitudinal variation in TEC outside of the depletion decreases significantly over time. The boundary condition issue could be rectified in future by using global GITM runs with local grid refinement, a capability for investigating multi-scale phenomena described by Zhao et al. (2020).

6 Conclusions

Ionospheric depletions were observed following the launch of an Electron SLLV. Observations and GITM simulations of STEC changes due to these depletions were comparable in magnitude and duration, demonstrating the promise of GCMs for modelling these anthropogenic impacts upon the ionosphere. Simulations indicated that exhaust gasses were short-lived compared with the resulting ionospheric depletion, unlike the FORMOSAT-5 launch case previously examined by Bowden et al. (2020). Evidence was found in GNSS observations for southward advection of the ionospheric depletion, which was not accounted for in the regional GITM simulation. These findings will inform future GCM development for simulating interactions between rockets and the ionosphere.

Acknowledgments
This work was carried out with funding from the Air Force Office of Scientific Research (award number FA2386-22-1-4003). Resources from the National Computational Infrastructure (NCI), supported by the Australian Government, were used. MAPGPS TEC data were obtained through the Madrigal CEDAR Database,accessible via the World Wide Web (at `http://cedar.openmadrigal.org/index.html/`).

References

Booker, H. (1961). A local reduction of F-region ionization due to missile transit. *Journal of Geophysical Research*, *66*(4), 1073–1079. Retrieved from `http://dx.doi.org/10.1029/jz066i004p01073` doi: 10.1029/jz066i004p01073

Bowden, G. W., Lorrain, P., & Brown, M. (2020). Numerical simulation of ionospheric depletions resulting from rocket launches using a general circulation model. *Journal of Geophysical Research: Space Physics*, *125*(6), e2020JA027836.

Furuya, T., & Heki, K. (2008). Ionospheric hole behind an ascending rocket observed with a dense GPS array. *Earth, Planets and Space*, *60*(3), 235–239. Retrieved from http://dx.doi.org/10.1186/BF03352786 doi: 10.1186/BF03352786

Jarvinen, P. O., Hill, J. A. F., Draper, J. S., & Good, R. E. (1966). *High altitude rocket plumes* (Tech. Rep.). MITHRAS, Cambridge.

Matzka, J., Bronkalla, O., Tornow, K., Elger, K., & Stolle, C. (2021). Geomagnetic kp index. *GFZ German Research Centre for Geosciences*, *11*.

Mendillo, M. (1981). The effect of rocket launches on the ionosphere. *Advances in Space Research*, *1*(2), 275–290. Retrieved from http://dx.doi.org/10.1016/0273-1177(81)90302-1 doi: 10.1016/0273-1177(81)90302-1

Mendillo, M., & Baumgardner, J. (1982). Optical signature of an ionospheric hole. *Geophysical Research Letters*, *9*(3), 215–218. Retrieved from http://dx.doi.org/10.1029/GL009i003p00215 doi: 10.1029/GL009i003p00215

Mendillo, M., Hawkins, G. S., & Klobuchar, J. A. (1975). A sudden vanishing of the ionospheric F region due to the launch of skylab. *Journal of Geophysical Research*, *80*(16), 2217–2228. Retrieved from http://dx.doi.org/10.1029/JA080i016p02217 doi: 10.1029/JA080i016p02217

Park, J., Kil, H., Stolle, C., Lühr, H., Coley, W. R., Coster, A., & Kwak, Y. S. (2016). Daytime midlatitude plasma depletions observed by Swarm: Topside signatures of the rocket exhaust. *Geophysical Research Letters*, *43*(5), 1802–1809. Retrieved from http://dx.doi.org/10.1002/2016GL067810 doi: 10.1002/2016GL067810

Ridley, A. J., Deng, Y., & Tóth, G. (2006). The global ionosphere-thermosphere model. *Journal of Atmospheric and Solar-Terrestrial Physics*, *68*(8), 839-864. Retrieved from http://dx.doi.org/10.1016/j.jastp.2006.01.008 doi: 10.1016/j.jastp.2006.01.008

Rocket Lab. (2021). *Rocket lab - they go up so fast launch 03/22/2021.* Retrieved from https://www.youtube.com/watch?v=u5wmrGriVX0

Rocket Lab. (2022). *Electron.* Retrieved 2022-12-6, from https://www.rocketlabusa.com/launch/electron/

Tapping, K. (2013). The 10.7 cm solar radio flux (f10. 7). *Space weather*, *11*(7), 394–406.

Wand, R. H., & Mendillo, M. (1984). Incoherent scatter observations of an artificially modified ionosphere. *Journal of Geophysical Research: Space Physics*, *89*(A1), 203–215. Retrieved from http://dx.doi.org/10.1029/JA089iA01p00203 doi: 10.1029/JA089iA01p00203

Zhao, Y., Deng, Y., Wang, J.-S., Zhang, S.-R., & Lin, C. Y. (2020). Tropical cyclone-induced gravity wave perturbations in the upper atmosphere: Gitm-r simulations. *Journal of Geophysical Research: Space Physics*, *125*(7), e2019JA027675.

Numerical Simulation of Rocket Generated Travelling Ionospheric Disturbances Using a General Circulation Model

G. W. Bowden [1]

[1] *School of Engineering and Information Technology, University of New South Wales Canberra, Northcott Drive, Campbell, Australian Capital Territory, 2612, Australia*

Summary: Rocket exhaust plumes generate acoustic and gravity waves in the upper atmosphere. These waves drive travelling ionospheric disturbances (TIDs) which can be observed, for example, in measurements of total electron content (TEC) from navigation satellite signals. The Global Ionosphere Thermosphere Model (GITM) was used to model acoustic wave propagation and ionospheric interaction. GITM boundary conditions incorporated perturbations computed using a ray tracing model with an analytically calculated source representing the rocket exhaust plume. This ray tracing model accounted for neutral winds and non-linear aging.

The Jason-3 launch on a Falcon 9 rocket was simulated using these methods. GITM wave propagation was compared with ray tracing simulation output based on arrival times and pressure perturbations. Ionospheric disturbances above and below the trajectory were examined using GITM and related to thermospheric perturbations. TEC estimates from this method were compared with those measured using navigation satellite signals in a previous study.

Keywords: acoustic ray tracing, general circulation model, shock acoustic waves, ionospheric disturbance.

Introduction

Rocket launches have been shown to impact the ionosphere in various ways, as summarised in reviews by Mendillo [1] and Afraimovich *et al.* [2]. These disturbances include effects of atmospheric waves which are generated by the expansion of rocket exhaust plumes. Such TIDs have been observed, for example, in ionosonde [3], incoherent scatter radar [4], very long baseline interferometer [5], and Global Navigation Satellite System (GNSS) ground station [6, 7, 8] ionosphere measurements. These TIDs propagate with a wide range of periods and group velocities and have been associated with shock acoustic waves (SAWs), atmospheric gravity waves, and ducted gravity waves.

Waves in the thermosphere drive ionospheric perturbations in several ways resulting from ion-neutral collisions and changes in reaction rates [9]. Firstly, the entrainment of ions by neutral gas can produce compressions and rarefactions in their density. Moreover, this motion can move ions along magnetic field lines to different altitudes, changing loss rates. Changes in neutral gas densities at a point in the thermosphere can also change ion production rates there as well as solar extreme ultraviolet (EUV) radiation fluxes beneath it. Finally, ions being dragged perpendicular to magnetic field lines by neutral gas can produce potential differences which get mapped along the field lines [10]. Resulting polarisation electric fields can then

affect ion motion at different altitudes. The relative importance of each of these mechanisms is strongly dependent on altitude [9].

Lin et al. described a set of GNSS observations of ionospheric disturbances following a rocket launch [7]. Two-dimensional TEC variation maps were derived assuming ionospheric pierce points at 200 km altitude, the approximate altitude achieved by the rocket during its second stage firing. V-shaped perturbations in the time rate of change of TEC were identified which propagated away from the rocket trajectory. These perturbations were attributed to SAWs.

TIDs generated by rockets offer a potential means of launch detection and characterisation. They may also help constrain properties of the ionosphere and thermosphere. Propagation velocities of the atmospheric waves are determined by temperature, neutral wind, and composition in the thermosphere. Ionospheric profiles also influence the disturbances through the mechanisms outlined above. While there have been extensive observations of TIDs generated by rockets, modelling has been limited. Previously, ray tracing has been used with simplified models of ion advection [5, 11] or assumed neutral wave perturbations have been used with ionospheric models [10].

This paper describes simulations of SAWs following the launch of the Jason-3 satellite. A general circulation model (GCM) for the ionosphere-thermosphere system was used to model wave propagation and ion-neutral interactions in detail. SAWs were introduced via boundary conditions obtained by acoustic ray tracing. Details of these models are provided in the Methods section. Ray tracing and GCM modelling of wave propagation is compared in the Results section, along with predicted ionospheric disturbances from the latter. Interpretation, limitations, and potential extensions are considered in the Discussion section.

Methods

Case Study Details

This study numerically modelled the SAWs detected by Lin et al. [7]. These disturbances were generated by the launch of a SpaceX Falcon 9 v1.1 rocket occurring at 18:42:18 UT (10:42:18 LT) on 17 January 2016. The launch took place from Space Launch Complex 4 East at Vandenberg Air Force Base (34.633°N, 120.613°W). Main engine cut-off occurred 154 s after lift-off and the second stage fired between 165 s and 540 s after lift-off [12]. The Jason-3 satellite was inserted into an initial near-polar low Earth orbit (inclination 60.04°) with approximately 200 km altitude. The trajectory for this launch was estimated previously by Bowden et al. [13], for a study of chemical ionospheric depletions rather than waves. Solar and geomagnetic activity were low at the time of the launch, with a daily F10.7 flux of 101 SFU measured at Penticton Radio Observatory[1] and Potsdam 3-hourly Kp-index of 1-[2].

Acoustic Ray Tracing

Acoustic ray tracing computes propagation of the waves through a medium by idealising these as a collection of infinitesimally wide beams. It relies upon the assumption of geometric acoustics; that is, the wavelength is very small compared with the length scales of the problem

[1] *Solar radio flux - archive of measurements*, Space Weather Canada, https://www.spaceweather.gc.ca/forecast-prevision/solar-solaire/solarflux/sx-5-en.php
[2] Matzka, Jürgen, et al. *Geomagnetic Kp index*. V. 1.0. GFZ Data Services. https://doi.org/10.5880/Kp.0001

under consideration. Also implicit in this technique is the assumption that the medium can be treated as a fluid; having a mean free path which is very small compared with the wavelength.

In the present work, ray tracing in an inhomogeneous moving atmosphere is implemented based on the Hamiltonian system of equations derived by Uginčius [14]. These were converted to spherical coordinates and solved using MATLAB's ode45 solver. This treatment neglected buoyancy effects, corresponding to the assumption that the acoustic wave period, T, was much shorter than the Brunt–Väisälä period,

$$T_b = 2\pi / \sqrt{(g \cdot (\gamma - 1) / (\gamma \cdot H) + (g / \tau) \cdot (d\tau / dz))}. \quad (1)$$

Here H is scale height, γ is isentropic expansion factor, g is downward gravitational acceleration, τ is temperature, and z is altitude.

An acoustic ray tracing simulation was carried out for the Jason-3 launch. Rays were launched at 10 points along the rocket trajectory at regular time intervals from 160 s to 400 s after launch. This covered the period of ascent during the second stage firing, which has previously been associated with SAW generation [15]. At each point, $N_\alpha = 25$ rays were launched above the horizontal and 25 rays were launched below the horizontal. The rays were launched at an angle to the rocket trajectory complementary to the Mach angle, μ. The azimuthal angle for the projection of ray i onto a plane perpendicular to the trajectory was given by,

$$\alpha_i = \pm(\pi / 2) \cdot (2 - 1 / (\lceil N_\alpha / 2 \rceil - i + 1)), \text{ for } i = 1, \ldots, \lceil N_\alpha / 2 \rceil \quad (2)$$
$$\alpha_i = \pm(\pi / 2) \cdot (1 / (i + 1 - \lceil N_\alpha / 2 \rceil)), \text{ for } i = \lceil N_\alpha / 2 \rceil + 1, \ldots, N_\alpha. \quad (3)$$

This preferentially launched rays near the horizontal, which tended to increase their coverage at a given altitude, as shown in Fig. 1. Atmospheric quantities, such as τ and γ were determined using the NRLMSISE-00 empirical model of the upper atmosphere [16]. Neutral winds were computed based on the HWM07 empirical horizontal wind model [17].

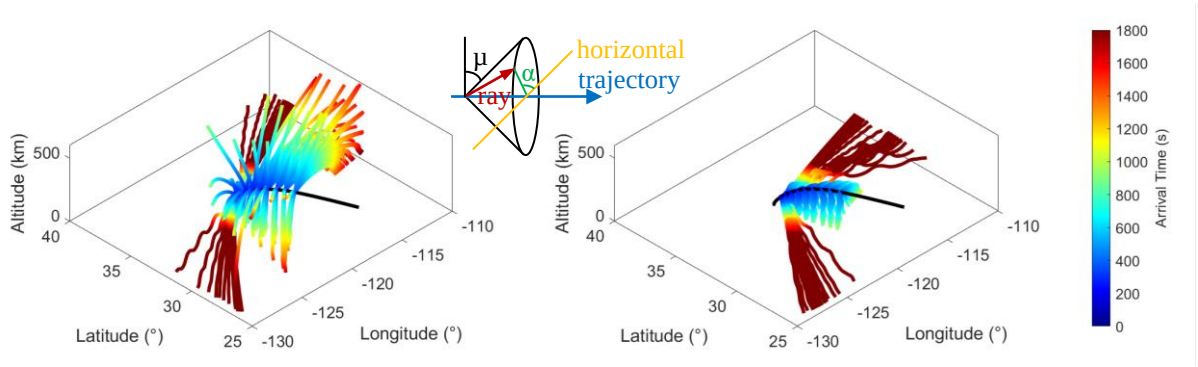

(a) (b)

Fig. 1: Arrival time of (a) initially upward ($0° < \alpha_i < 180°$) and (b) initially downward ($-180° < \alpha_i < 0°$) acoustic rays for the Jason-3 launch, shown with rocket trajectory (black line). Inset: ray launch geometry.

Fig. 1 shows the trajectory and arrival time for acoustic rays in the simulation. The thermal gradient in the thermosphere implied that there was a gradient in sound speed,

$$c_s = \sqrt{(\gamma \cdot k_B \cdot \tau / m)}, \quad (4)$$

where k_B is Boltzmann's constant and m is the mean molecule mass. This resulted in downward refraction of the rays. The minimum in temperature and sound speed around the mesopause caused ducting of slowly travelling rays around 90 km altitude. Some asymmetry in ray propagation occurred due to north-westward neutral winds.

Analytic methods were used to estimate pressure, temperature, and velocity perturbations along the rays. The theoretical treatment of Jarvinen et al. was adopted to determine dimensions of the plume [18]. This was approximated as an equivalent parabolic solid of revolution, as illustrated in Fig. 2. Near-field pressure perturbations generated by this supersonic body were calculated using the weakly nonlinear theory of Whitham [19] as applied by Middleton et al. [20]. This describes evolution (or "ageing") of the perturbations towards the N-wave profile in the far field. Conservation of energy was ensured by requiring that the Blokhintzev parameter remain constant along rays [21]. Velocity and density perturbations were computed from pressure perturbations using a plane wave assumption.

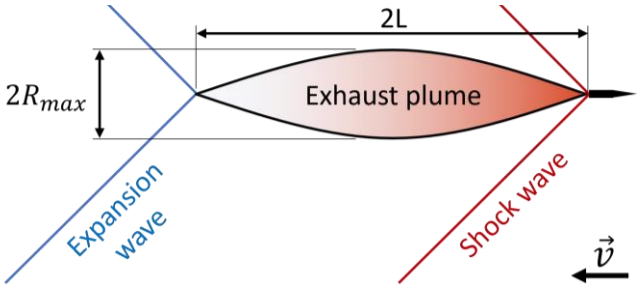

Fig. 2: Dimensions and assumed shape of the exhaust plume (rocket rest frame).

Global Ionosphere Thermosphere Model

The Global Ionosphere Thermosphere Model (GITM) is a GCM which simulates the major ionised and neutral components of the upper atmosphere [22]. This model numerically solves coupled continuity, momentum, and energy equations for the ionosphere and thermosphere on a three-dimensional grid. Terms are included representing gravity, external electromagnetic fields, EUV photoionisation and photodissociation, auroral particle precipitation, and ionosphere/thermosphere chemistry. The model separates vertical and horizontal advection, based on the difference in typical vertical and horizontal length scales in the upper atmosphere. GITM differs from other GCMs in that it does not assume hydrostatic equilibrium in the vertical direction, adopting altitude rather than pressure level as the vertical coordinate [22]. This feature allows GITM to model acoustic waves [23].

GITM can be run either for the entire globe or a region bounded in latitude and longitude. The latter mode was used in this work, permitting high resolution of the region of interest without excessive computational requirements. In this mode, GITM set zonal and meridional gradients in variables to zero at its longitude and latitude boundaries, respectively. The simulations covered a domain of 123°W to 113°W and 28°N to 36°N, with 160 by 160 grid points. Lower thermosphere simulations covered 100 to 165 km altitude and upper thermosphere simulations covered 225 to 600 km altitude, with grid points spaced at 5 km intervals (comparable with the horizontal spacing). The GITM three-dimensional electrodynamics model was not used, thereby neglecting effects of polarisation electric fields induced by SAWs.

GITM was initialised using the NRLMSISE-00 thermosphere, HWM07 neutral wind, and IRI ionosphere [24] empirical models. The simulations began at 18:40 UT 17 January 2016 and concluded at 19:10 UT. This period was very short compared with the typical 1.5 days for

GITM to converge on a solution independent of initial conditions [22]. Thus, the unperturbed state overwhelmingly reflected the empirical models used to initialise the simulations rather than the dynamics of GITM. Fig. 3 shows vertical profiles derived from the empirical models.

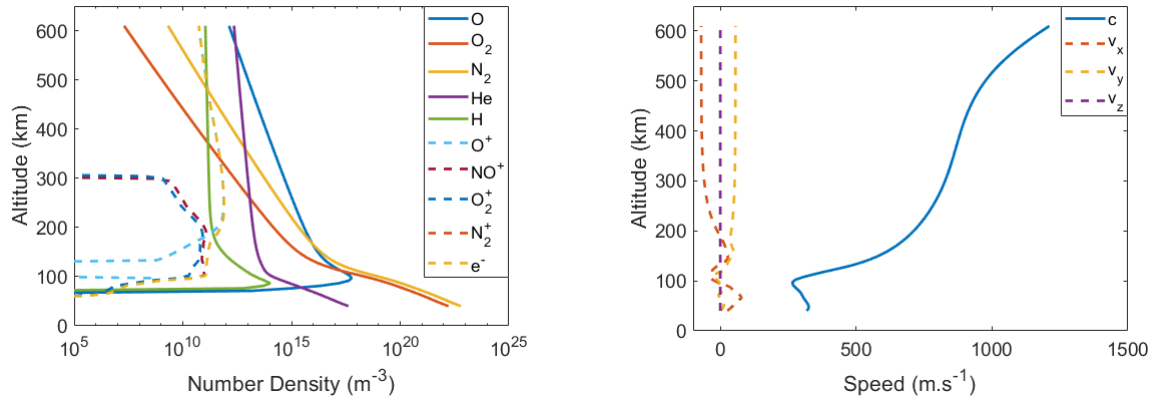

(a) (b)

Fig. 3: (a) Vertical profiles of NRLMSISE-00 neutral number densities (solid) and IRI ion and electron number densities (dashed). (b) Vertical profiles of HWM07 neutral wind velocity components (dashed, x is east, y is north, and z is up) and sound speed (from NRLMSISE-00). All profiles were taken at (32°N, 118°W) for 18:50 UT.

Fig. 4 shows vertical profiles of length and time scales computed by the empirical models. It suggests the assumptions of the acoustic ray tracing method held for most of the upper atmosphere. The length scale of the plume, L, is substantially greater than the mean free path, l, and less than acoustic cut-off wavelength, λ_a, or the scale height for changes in sound speed, $H_c = c \,/\, |dc \,/\, dz|$, except around 120 km altitude. The time period, $T = 2L \,/\, u$ where u is the rocket speed, is much less than the acoustic cut-off period, T_a, or Brunt-Väisälä period, T_b.

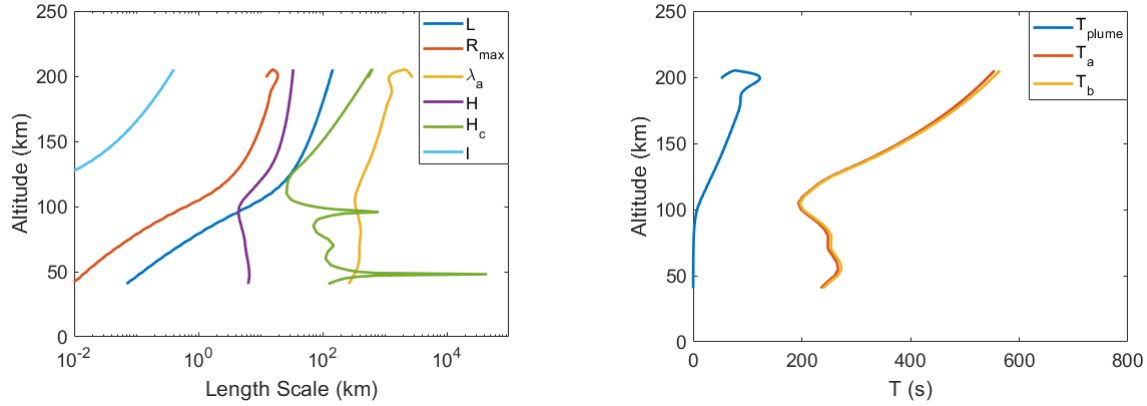

(a) (b)

Fig. 4: (a) Length scales and (b) time scales along the rocket trajectory.

Upper and Lower Boundary Conditions

Acoustic ray tracing simulation results were used to compute perturbations to density, ρ, temperature, τ, and neutral wind velocity, $\boldsymbol{v}$, at the GITM vertical ghost-cells. These were applied to the upper boundary for lower thermosphere simulations and the lower boundary for upper thermosphere simulations. Computing these perturbations involved interpolation from the irregularly spaced points where rays pierced a constant altitude surface to the grid points

at that altitude. This was done using the griddata MATLAB function. As indicated by Fig. 1, only initially upward propagating rays reached the lower boundary of the upper thermosphere simulation, while those which reached the upper boundary of the lower thermosphere simulation included both initially upward and downward propagating rays.

Results

Comparison of Acoustic Ray Tracing and GITM

Arrival times for SAW perturbations were comparable for ray tracing and GITM simulations, as shown in Fig. 5. Ray-tracing arrival times represented the leading edge of disturbances and GITM arrival times when density disturbances reached 10% of their maximum value. At altitudes of 150 km and 250 km, similar V-shaped arrival time contours were evident, suggesting that acoustic wave propagation speed and direction agreed between simulations. Truncation of the V-shape in Fig. 5(d), reflected when the simulated source turned off.

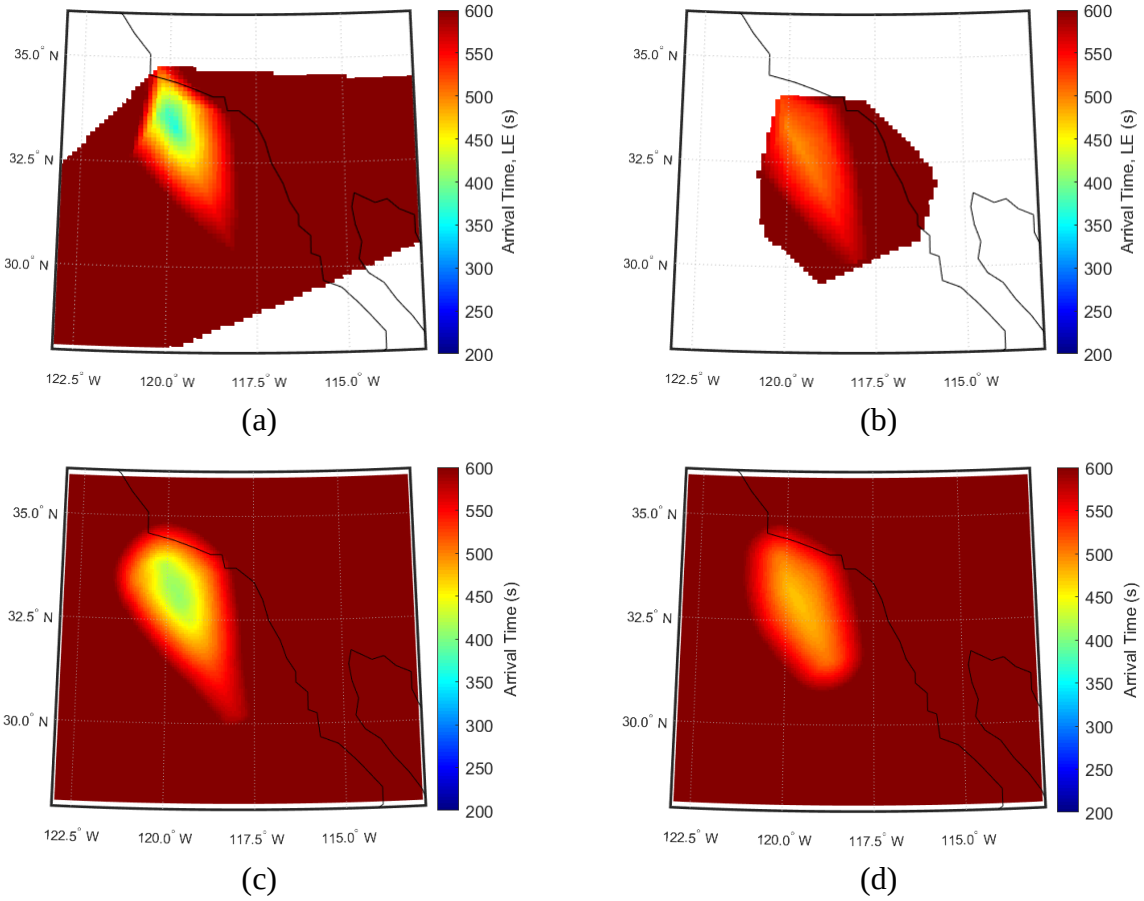

Fig. 5: SAW arrival time from ray tracing (a) at 150 km and (b) at 250 km altitude and from GITM (c) at 150 km and (d) at 250 km altitude. Dark red denotes arrival after 600 s.

Fig. 6 and Fig. 7 show SAW neutral density perturbations from each simulation and SAW electron number density perturbations from the GITM simulation at 150 km and 250 km respectively. There was reasonable agreement between simulations regarding the spatial pattern of density perturbations, and hence also for propagation direction and wavelength. However, GITM estimated substantially smaller neutral density perturbations than ray tracing. Moreover, these perturbations were more smoothed out in the former case. At 150 km, neutral

density perturbations coincided with opposite signed electron number density perturbations. By contrast, at 250 km, electron number density perturbations tended to have the same sign as neutral density perturbations and the former persisted in the wake of the latter. Perturbations travelling to the rocket's left were larger than those travelling to the right in the GITM output.

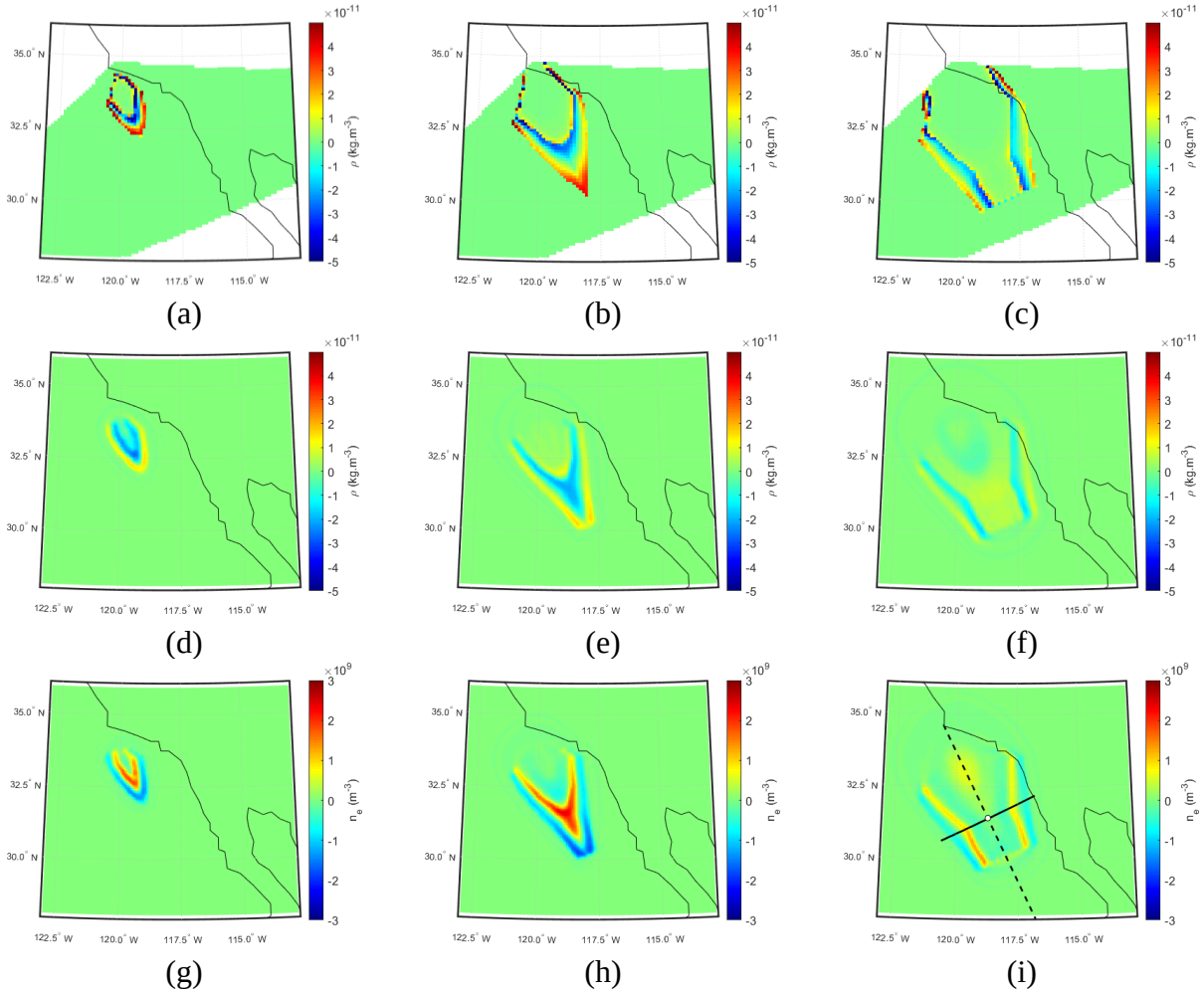

Fig. 6: Perturbation maps at 150 km altitude for (first row) ray tracing density, (second row) GITM density, and (third row) GITM electron number density. Taken at (first column) 18:48 UT, (second column) 18:50 UT, and (third column) 18:52 UT.

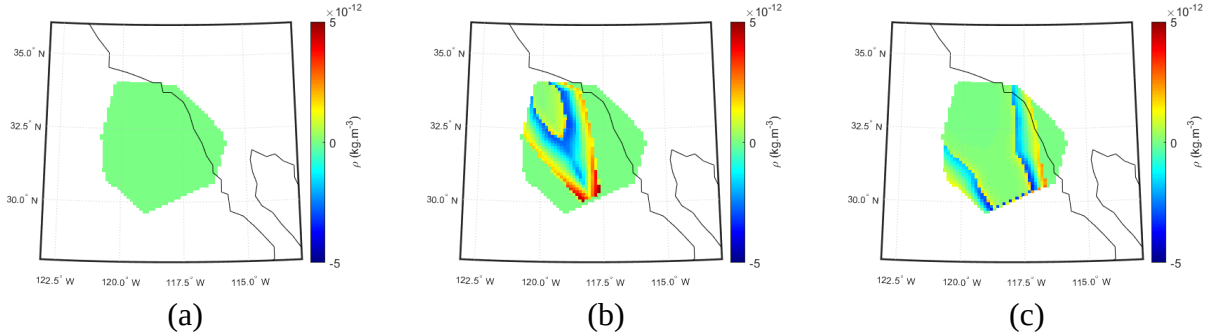

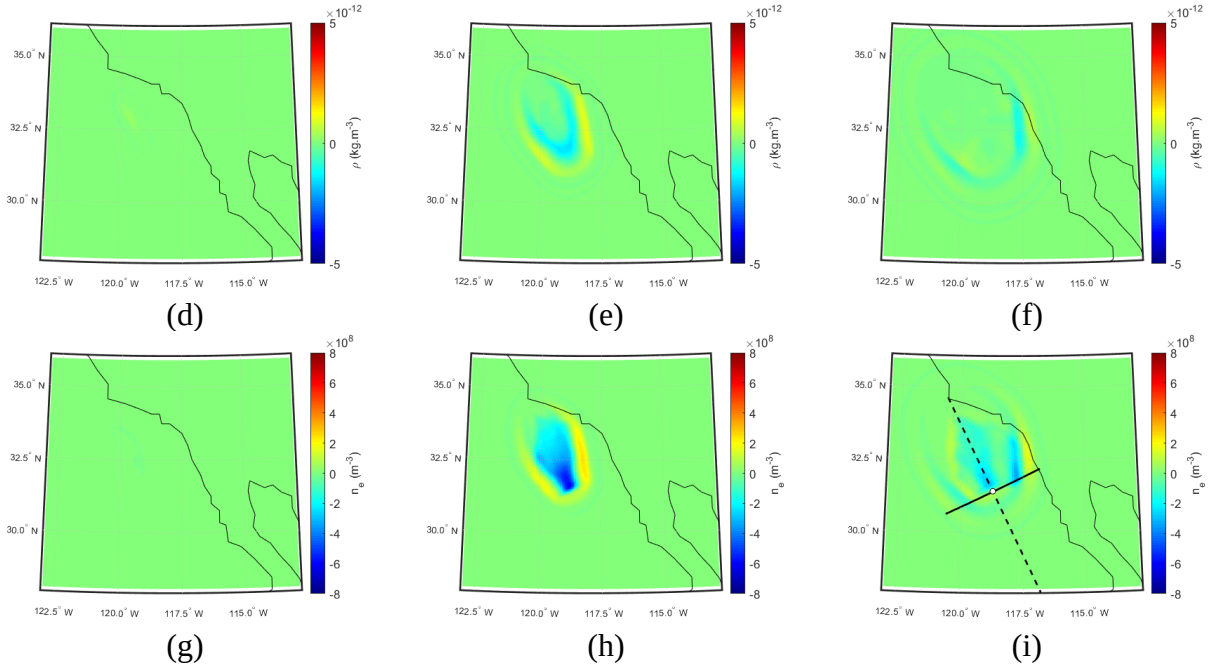

Fig. 7: Perturbation maps at 250 km altitude for (first row) ray tracing density, (second row) GITM density, and (third row) GITM electron number density. Taken at (first column) 18:48 UT, (second column) 18:50 UT, and (third column) 18:52 UT.

Propagation of Thermosphere and Ionosphere Perturbations

Vertical and horizontal propagation of SAW perturbations are shown in Fig. 8. Fig. 8(a) and (b) show temporal evolution of altitude profiles for temperature and electron number density perturbations at a point on the ground track, (31.425°N, 118.71875°W) respectively marked by a white dot and dashed line on Fig. 6(i). In the former plot, SAW vertical phase velocity increased with altitude. This qualitative behaviour was expected from the sound speed Fig. 3(b), though GITM propagation speeds were significantly higher (0.6 km.s^{-1} at 100-150 km, 1.7 km.s^{-1} at 250-350 km, and 14 km.s^{-1} at 500-600 km).

Temperature perturbations declined more slowly moving upward from the source than downward, as expected for the stratified atmosphere in Fig. 3(a). Above the F-region peak in Fig. 3(a), positive electron density perturbations occur between SAW temperature (and hence density) maxima and minima. Immediately below, this relationship is reversed. A small increase in electron number density occurs around 240 km in the wake of the SAW. In the lower thermosphere, electron number density perturbations do not follow acoustic wave propagation and appear rapidly across a range of altitudes.

TEC changes along a line perpendicular to the ground track in the lower and upper thermosphere are shown in Fig. 8(c) and (d) respectively. Initial TEC perturbations are negative for the lower thermosphere and typically positive for the upper thermosphere. For both the upper and lower thermosphere, propagation was asymmetric about the ground track, with a higher along-line velocity to the left of the rocket. For the lower thermosphere this approached about 1.4 km.s^{-1} to the left and 0.9 km.s^{-1} to the right, and for the upper thermosphere this approached about 1.4 km.s^{-1} to the left and 0.8 km.s^{-1} to the right.

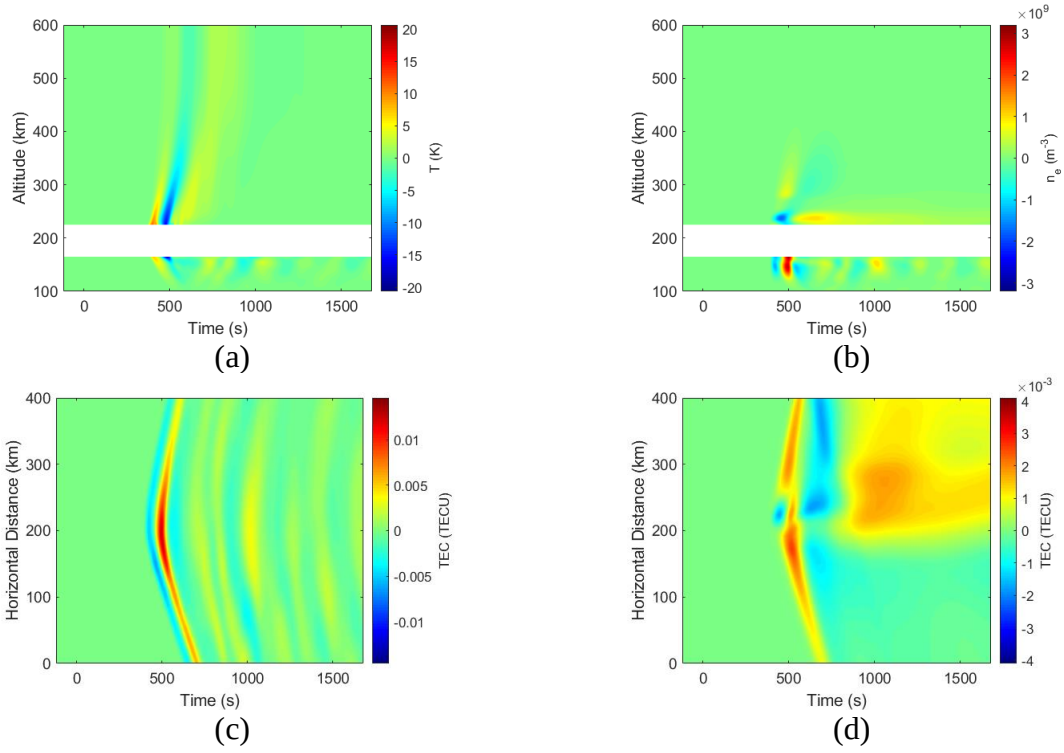

Fig. 8: Vertical and horizontal propagation of perturbations. (a) Temperature and (b) electron number density perturbations at the white circle in Fig. 6(i). TEC perturbations in the (c) lower and (d) upper thermosphere along the solid black line in Fig. 6(i), measuring distances from the SW end of the line.

Discussion

GITM SAW simulations showed V-shaped disturbances qualitatively similar to those derived from GNSS measurements [7]. Those measurements indicated that initial TEC changes were positive, like the simulated electron number density changes in the upper thermosphere but unlike those in the lower thermosphere. This suggests that upper ionosphere perturbations were predominantly responsible for the observed SAW TEC signature.

SAW TEC perturbations were approximately an order of magnitude smaller in GITM than GNSS measurements (comparing Fig. 8 of this paper with Fig. 3 from Lin et al. [7]). This may have been partly attributable to underestimation of SAW thermosphere perturbations in GITM (suggested by comparison with ray tracing in Fig. 6 and Fig. 7). Numerical diffusion and difficulty capturing shocks in the GITM advection scheme likely contributed to this underestimation. Also, perturbations around 200 km were not included in simulations but may have contributed significantly to observations, given that ionosphere perturbations were greatest near the perturbed simulation boundaries.

The time when disturbances appeared in the simulations differed from Lin et al. [7], apparently resulting from use of a non-causal filter in the latter. At 252 s after launch, Fig. 1 in that reference shows the SAW wavefronts approximately 530 km horizontally from the launch site. However, integration under the curve in Fig. 5(a) of Chou et al. [8] indicates that the rocket had only travelled approximately 250 km in total at this time. If the pierce point altitude associated with ionospheric perturbations were overestimated the distance to pierce

points would also be overestimated. This would place the wavefronts further from the land based GNSS ground stations than they actually were.

Several factors could have contributed to the asymmetry seen in Fig. 8(c) and (d). Possible physical causes may have included orientation with respect to the (north-westward) neutral winds and (northward) magnetic field lines. Numerical causes may have included orientations with respect to the grid and asymmetry of the region where perturbations were applied. The rightward SAW velocity components were comparable to those indicated in Fig. 3 of Lin et al. [7]. However, an 8-15 min bandpass filter was applied to those results and the periods reported were much greater than those for simulations presented here.

The relationship between SAW perturbations in the thermosphere and ionosphere varies with altitude due to changing collision, reaction, and photoionisation rates. In the upper thermosphere, compressions (rarefactions) in neutral species cause compressions (rarefactions) in long lived ions moving along magnetic field lines. In the lower thermosphere, where O_2 and N_2 deplete O^+ via charge exchange and dissociative recombination, compressions (rarefactions) caused increased (decreased) loss rates. Moreover, compressions (rarefactions) reduced (increased) EUV fluxes reaching lower altitudes and thus production rates. Note that flux values were overestimated at the top of the lower thermosphere simulation, due to the neglect of EUV absorption above 165 km. While the TEC measurements available for this case do not distinguish ionosphere perturbations at different altitudes clearly, it may be possible to measure perturbations at specific altitudes with satellite Langmuir probe or ionosonde measurements.

The methodology presented here could be extended in several ways. Use of GITM with the three-dimensional electrodynamics model would allow consideration of polarisation electric field effects. GITM could be modified to run with the thermosphere state specified using NRLMSISE-00 and perturbations computed using ray tracing. This would remove unwanted non-equilibrium effects and numerical damping of SAWs. It would also allow the region around the source altitude to be included in the simulation. Finally, a different ray tracing simulation could be used to compute boundary condition perturbations representing atmospheric gravity waves.

Conclusion

This work used the GITM GCM to investigate propagation of SAWs due to rocket launches and the relationship between the resulting thermosphere and ionosphere perturbations. GITM showed promise as a model of these disturbances, producing reasonable estimates for SAW propagation and spatial profiles. SAW ionosphere perturbations extended over a range of altitudes and involved different mechanisms, though appeared to be greatest near the source altitude.

Acknowledgements

Many thanks to Professor Aaron Ridley of University of Michigan for helpful communications regarding the GITM code, including identification of the source of the “strobing” problem in earlier electron density results. Thanks also to Dr. Melrose Brown for useful discussions regarding the results presented here. Support from the Asian Office of

Aerospace Research and Development is gratefully acknowledged (award number FA2386-22-1-4003).

References

1. Mendillo, M. "The Effect of Rocket Launches on the Ionosphere", *Advances in Space Research*, Vol. 1, No. 2, 1981, pp. 275-290.

2. Afraimovich, E.L., Astafyeva, E.I., Demyanov, V.V., Edemskiy, I.K., Gavrilyuk, N.S., Ishin, A.B., Kosogorov, E.A., Leonovich, L.A., Lesyuta, O.S., Palamartchouk, K.S. and Perevalova, N.P., "A review of GPS/GLONASS studies of the ionospheric response to natural and anthropogenic processes and phenomena.", *Journal of Space Weather and Space Climate*, Vol. 3, 2013, p. A27.

3. Arendt, P.R., "Ionospheric undulations following Apollo 14 launching", *Nature*, Vol. 231, No. 5303, 1971, pp. 438-439.

4. Noble, S.T., "A large-amplitude traveling ionospheric disturbance excited by the space shuttle during launch", *Journal of Geophysical Research: Space Physics*, Vol. 95, No. A11, 1990, pp. 19037-19044.

5. Li, Y.Q., Jacobson, A.R., Carlos, R.C., Massey, R.S., Taranenko, Y.N. and Wu, G., "The blast wave of the Shuttle plume at ionospheric heights", *Geophysical Research Letters*, Vol. 21, No. 24, 1994, pp. 2737-2740.

6. Calais, E. and Bernard Minster, J., "GPS detection of ionospheric perturbations following a Space Shuttle ascent", *Geophysical Research Letters*, Vol. 23, No. 15, 1996, pp. 1897-1900.

7. Lin, C.C., Shen, M.H., Chou, M.Y., Chen, C.H., Yue, J., Chen, P.C. and Matsumura, M., "Concentric traveling ionospheric disturbances triggered by the launch of a SpaceX Falcon 9 rocket", *Geophysical Research Letters*, Vol. 44, No. 15, 2017, pp. 7578-7586.

8. Chou, M.Y., Shen, M.H., Lin, C.C., Yue, J., Chen, C.H., Liu, J.Y. and Lin, J.T., "Gigantic circular shock acoustic waves in the ionosphere triggered by the launch of FORMOSAT-5 satellite", *Space Weather*, Vol. 16, No. 2, 2018, pp. 172-184.

9. Hooke, W.H., "Ionospheric irregularities produced by internal atmospheric gravity waves", *Journal of Atmospheric and Terrestrial Physics*, Vol. 30, No. 5, 1968, pp. 795-823.

10. Chou, M.Y., Lin, C.C., Shen, M.H., Yue, J., Huba, J.D. and Chen, C.H., "Ionospheric Disturbances Triggered by SpaceX Falcon Heavy", *Geophysical Research Letters*, Vol. 45, No. 13, 2018, pp. 6334-6342.

11. Bowling, T., Calais, E. and Haase, J.S., "Detection and modelling of the ionospheric perturbation caused by a Space Shuttle launch using a network of ground-based Global Positioning System stations", *Geophysical Journal International*, Vol. 192, No. 3, 2013, pp. 1324-1331.

12. SpaceX, *Jason-3 Mission*, Accessed November 1, 2022, https://spacex.com.pl/files/2017-10/jason-3-press-kit.pdf.

13. Bowden, G.W., Lorrain, P. and Brown, M., "Numerical Simulation of Ionospheric Depletions Resulting From Rocket Launches Using a General Circulation Model", *Journal of Geophysical Research: Space Physics*, Vol. 125, No. 6, 2020, p. e2020JA027836.

14. Uginčius, P., "Ray acoustics and Fermat's principle in a moving inhomogeneous medium", *The Journal of the Acoustical Society of America*, Vol. 51, No. 5B, pp. 1759-1763.

15. Lin, C.H., Lin, J.T., Chen, C.H., Liu, J.Y., Sun, Y.Y., Kakinami, Y., Matsumura, M., Chen, W.H., Liu, H. and Rau, R.J., "Ionospheric shock waves triggered by rockets", *Annales Geophysicae*, Vol. 32, No. 9, 2014, pp. 1145-1152.

16. Picone, J.M., Hedin, A.E., Drob, D.P. and Aikin, A.C., "NRLMSISE-00 empirical model of the atmosphere: Statistical comparisons and scientific issues", *Journal of Geophysical Research: Space Physics*, Vol. 107, No. A12, 2002, pp. SIA-15.

17. Drob, D.P., Emmert, J.T., Crowley, G., Picone, J., Shepherd, G.G., Skinner, W., Hays, P., Niciejewski, R.J., Larsen, M., She, C.Y. and Meriwether, J.W., "An empirical model of the Earth's horizontal wind fields: HWM07", *Journal of Geophysical Research: Space Physics*, Vol. 113, No. A12, 2008.

18. Jarvinen, P.O., Hill, J.A., Draper, J.S. and Good, R.E., 1966. *High altitude rocket plumes*. MITHRAS, Cambridge, MA, 1966.

19. Whitham, G.B., "The flow pattern of a supersonic projectile", *Communications on pure and applied mathematics*, 5(3), 1952, pp. 301-348.

20. Middleton, W.D., *A numerical method for calculating near-field sonic-boom pressure signatures*, NASA, 1965.

21. Blokhintzev, D., "The propagation of sound in an inhomogeneous and moving medium I.", *The Journal of the Acoustical Society of America*, Vol. 18, No. 2, 1946, pp. 322-328.

22. Ridley, A.J., Deng, Y. and Toth, G., "The global ionosphere–thermosphere model", *Journal of Atmospheric and Solar-Terrestrial Physics*, Vol. 68, No. 8, 2006, pp. 839-864.

23. Deng, Y., Richmond, A.D., Ridley, A.J. and Liu, H.L., "Assessment of the non-hydrostatic effect on the upper atmosphere using a general circulation model (GCM)", *Geophysical Research Letters*, Vol. 35, No. 1, 2008.

24. Bilitza, D., Rawer, K., Bossy, L., Kutiev, I., Oyama, K.I., Leitinger, R. and Kazimirovsky, E., *International reference ionosphere 1990*, National Space Science Data Center/World Data Center A for Rockets and Satellites, 1990.